PEROVKSITES

Supramolecular assembly of blue and green halide perovskites with near-unity photoluminescence

Cheng Zhu[1,2,3]†, Jianbo Jin[4]†, Zhen Wang[1], Zhenpeng Xu[1], Maria C. Folgueras[1,2,3], Yuxin Jiang[2,4], Can B. Uzundal[2,4], Han K. D. Le[2,4], Feng Wang[2,3,5], Xiaoyu (Rayne) Zheng[1,6], Peidong Yang[1,2,3,4]*

The metal-halide ionic octahedron is the optoelectronic unit for halide perovskites, and a crown ether–assisted supramolecular assembly approach can pack various ionic octahedra into tunable symmetries. In this work, we demonstrate near-unity photoluminescence quantum yield (PLQY) blue and green emission with the supramolecular assembly of hafnium (Hf) and zirconium (Zr) halide octahedral clusters. $(18C6@K)_2HfBr_6$ powders showed blue emission with a near-unity PLQY (96.2%), and green emission was also achieved with $(18C6@K)_2ZrCl_4Br_2$ powders at a PLQY of 82.7%. These highly emissive powders feature facile low-temperature solution-based synthesis conditions and maintain high PLQY in solution-processable semiconductor inks under ambient conditions, and they were used in thin-film displays and emissive three-dimensional–printed architectures that exhibited high spatial resolution.

Blue and green emission with high photoluminescence quantum yield (PLQY) is at the forefront of solid-state lighting and color display research. Although Si and Zn codoped GaN can exhibit a PLQY of 90% (*1*), these covalent semiconductors require high purity to prevent rapid nonradiative recombination at crystal structure defects (*2–5*) and rely on solid-state synthesis at elevated temperatures near 1000°C (*6*). As an alternative to covalent semiconductors, ionic halide perovskites have received attention given their high optical absorption coefficient (*7*), tunable bandgap (*8–10*), high defect tolerance (*11, 12*), and efficient photo- and electroluminescence (*13, 14*). For example, the blue and green emissive colloidal $CsPbCl_xBr_{3-x}$ quantum dots have exhibited PLQY values of ~80% (*15, 16*). In addition, low-dimensional halide perovskites like the n = 1 Ruddlesden-Popper phase $(C_6H_5CH_2NH_3)_2PbBr_4$ show blue emission with a PLQY of 79% (*17*). Despite the notable optoelectronic properties of lead-based halide perovskites, the toxicity of lead and the complex colloidal synthesis complicate large-scale applications. Moreover, suitable ligands are still needed to prevent aggregation of these low-dimensional nanostructures during use (*18*).

Recent studies have revealed that the optoelectronic properties of halide perovskites stem from the $[MX_6]^{n-}$ (where M is a metal cation and X is a halide anion) fundamental building blocks in the crystal structure (*19–21*), and, given the ionic nature and high chemical tunability of halide perovskite structures (*22*), different compositions and packing geometries of $[MX_6]^{n-}$ could be explored for light-emission applications. The vacancy-ordered double perovskite (A_2MX_6 phase) has been proposed to incorporate tetravalent metal cation octahedra, such as $[TeX_6]^{2-}$ (*23–25*), $[SnX_6]^{2-}$ (*26, 27*), and $[PtX_6]^{2-}$ (*28, 29*). Although the $[PbX_6]^{4-}$ octahedra are corner-shared in all three dimensions in the prototypical $CsPbX_3$ structure (*30*), the $[MX_6]^{2-}$ octahedra in the A_2MX_6 phase are isolated because a vacancy occupies every other M site in the crystal structure (*23*). A few $[MX_6]^{n-}$ emitters as well as some non-octahedral emitters (*31*) with high PLQY (~95%) have been identified with yellow emission, such as $[SnX_6]^{4-}$ (*32*). However, emission of high PLQY with shorter wavelengths is still very rare. The isolated nature of the octahedra affects their optoelectronic properties in that the strong coupling of the exciton with lattice vibrations greatly lowers the energy level of the exciton and forces it into transient self-trapped exciton (STE) states with a range of self-trapped energy levels (*33, 34*). As a result, the A_2MX_6 systems generally have broadband emissions with a large Stokes shift.

Although the A_2MX_6 phase has been widely studied in various compositions, octahedra with Hf^{4+} or Zr^{4+} centers, especially $[HfBr_6]^{2-}$ and $[ZrBr_6]^{2-}$ octahedra, have rarely been the subject of research (*35, 36*), even though they have interesting optoelectronic properties. Cs_2HfBr_6 crystals have a blue emission with the PL peak at 435 nm (*35*), and colloidal Cs_2ZrBr_6 nanocrystals have been demonstrated to have a green emission with a PLQY of 45% (*36*). There are several reasons why they are less explored. Theoretical (*37*) and experimental studies (*38*) have shown that the Hf^{4+} and Zr^{4+} metal centers are extremely air- and moisture-

sensitive in the A_2MX_6 phase. Their synthesis requires the vertical Bridgman-Stockbarger method at ~1000°C in sealed quartz ampoules (*36, 39, 40*). Finally, it is difficult to prepare high-purity samples that do not contain a secondary impurity, such as CsBr (*36*). Thus, a new methodology is needed for the synthesis of more stabilized and purer solid phases containing the $[HfBr_6]^{2-}$ or $[ZrBr_6]^{2-}$ octahedra.

Recently, we proposed a general crown ether–assisted supramolecular assembly approach for tetravalent metal octahedra (*41*). Two crown ether@alkali metal complexes can sandwich a tetravalent metal octahedron into a (crown ether@A)$_2MX_6$ dumbbell structural unit. The composition of the dumbbell structural unit is highly tunable, with crown ether = 18-crown-6 (18C6) or 21-crown-7 (21C7); A = Cs^+, Rb^+, or K^+; M = Te^{4+}, Sn^{4+}, Se^{4+}, Ir^{4+}, Pt^{4+}, Zr^{4+}, Hf^{4+}, or Ce^{4+}; and X = Cl^-, Br^-, or I^-. In this work, we extended this general supramolecular assembly approach to $[HfBr_6]^{2-}$ octahedra to achieve a structure with formula $(18C6@K)_2HfBr_6$ that features blue emission with near-unity (96.2%) PLQY. We also optimized the synthetic route by replacing the challenging high-temperature solid-state synthesis with a low-temperature organic solution–based synthesis. Moreover, an efficient green emission was also achieved by tuning the composition of the (crown ether@A)$_2MX_6$ dumbbell structural unit. $(18C6@K)_2ZrCl_4Br_2$ demonstrated green emission with 82.7% PLQY. By studying the photophysics of the supramolecular assembled samples, we could attribute the emission to STE states and observed a very strong electron-phonon coupling constant (represented by the Huang-Rhys parameter) of >90 for $(18C6@K)_2HfBr_6$. The supramolecular assembled samples had longer PL lifetimes (in the microsecond timescale) compared with those of other halide perovskite systems that reflected a low rate of nonradiative recombination.

The structural integrity and impressive optical properties of the supramolecular assembled solid powders were further maintained by generating a powder suspension in nonpolar organic solvents, such as dichloromethane (DCM), to create an ink system. Polystyrene (PS) polymer was dissolved into the ink to further increase the solution processability. We used these inks to fabricate thin films through fast solvent evaporation. In combination with a digitally controlled excitation source, the $(18C6@K)_2HfBr_6$/PS composite thin film could be used as a display with bright color contrast and fast response time. A solution-processable ink also allowed three-dimensional (3D) printing of the powders into various blue-, green-, and dual-color–emitting structures.

Crown ether–assisted supramolecular assembly

We explored a supramolecular synthetic route in which 18C6 greatly increased the solubility

[1]Department of Materials Science and Engineering, University of California Berkeley, Berkeley, CA 94720, USA. [2]Materials Sciences Division, Lawrence Berkeley National Laboratory, Berkeley, CA 94720, USA. [3]Kavli Energy NanoScience Institute, Berkeley, CA 94720, USA. [4]Department of Chemistry, University of California Berkeley, Berkeley, CA 94720, USA. [5]Department of Physics, University of California Berkeley, Berkeley, CA 94720, USA.USA. [6]Energy Technologies Area, Lawrence Berkeley National Laboratory, Berkeley, CA 94720, USA.
*Corresponding author. Email: p_yang@berkeley.edu
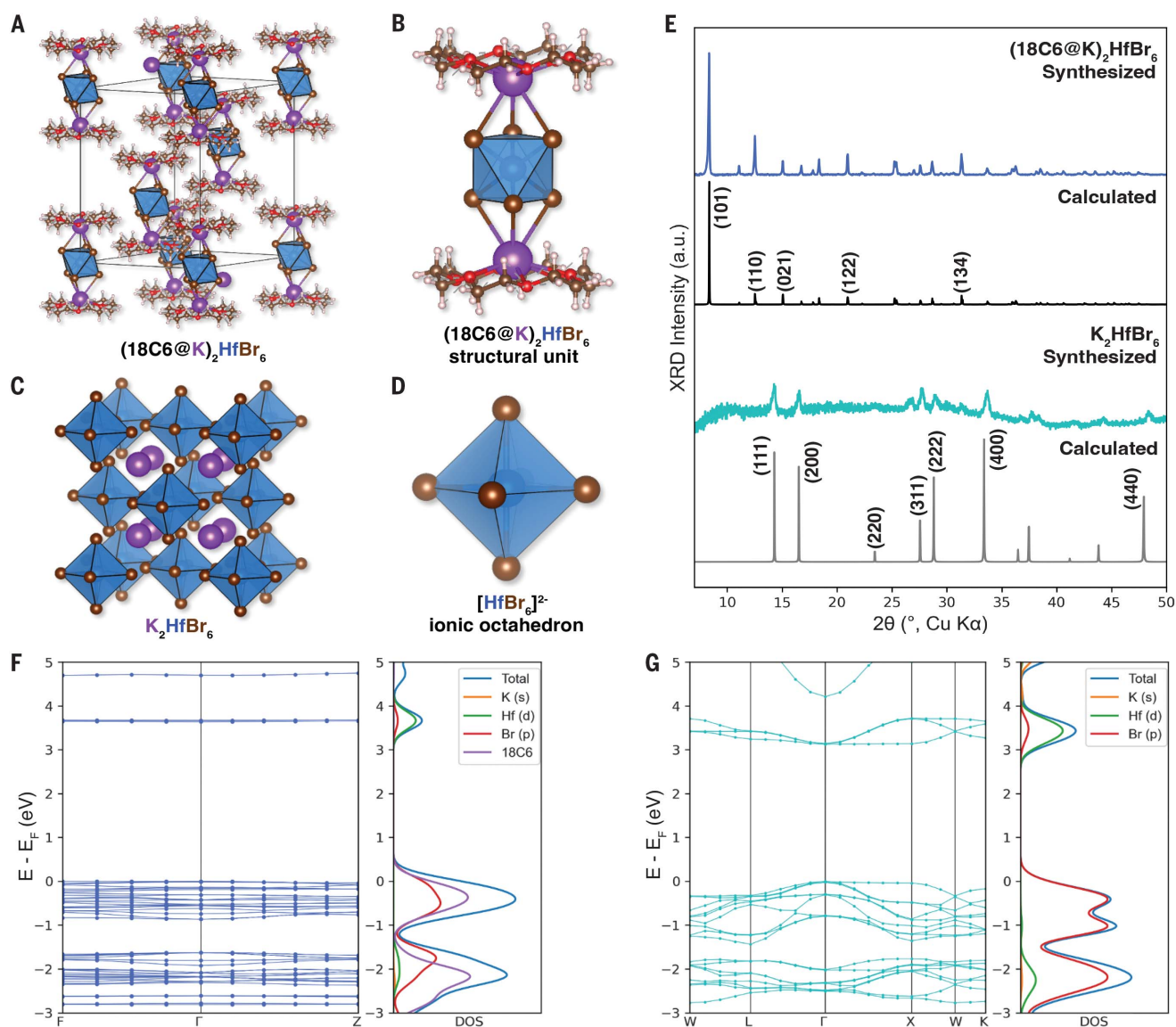†These authors contributed equally to this work.

Fig. 1. Two assemblies of the [HfBr$_6$]$^{2-}$ ionic octahedron. (**A** and **B**) The rhombohedral unit cell (A) and the dumbbell-shaped structural unit (B) of (18C6@K)$_2$HfBr$_6$. (**C** and **D**) The Fm-3m unit cell [from the Open Quantum Materials Database (OQMD) (*36*, *37*)] (C) and the isolated [HfBr$_6$]$^{2-}$ ionic octahedron building block (D) of K$_2$HfBr$_6$. (**E**) The PXRD patterns for synthesized (18C6@K)$_2$HfBr$_6$ and K$_2$HfBr$_6$ powders and the calculated diffraction patterns. K$_2$HfBr$_6$ showed quite poor PXRD quality because of its poor stability during measurement. a.u., arbitrary unit. (**F** and **G**) Band structure and corresponding total pDOS of (18C6@K)$_2$HfBr$_6$ (F) and K$_2$HfBr$_6$ (G). When [HfBr$_6$]$^{2-}$ octahedra were assembled in the supramolecular approach, the dispersion of the bands decreased, and 18C6 contributed to the VB.

of the KBr and HfBr$_4$ precursors in polar organic solvents for low-temperature solution-based synthesis. A clear precursor solution was obtained with acetonitrile (ACN) at 80°C with the concentration of 4 mM for 18C6 and KBr and 2 mM for HfBr$_4$. Our previous study of the supramolecular assembly of tetravalent metal octahedra (*41*) indicated that a (18C6@K)$_2$HfBr$_6$ dumbbell structural unit was formed in ACN. We grew (18C6@K)$_2$HfBr$_6$ powders and single crystals using the antisolvent crystallization method (*39*). K$_2$HfBr$_6$ powders were also synthesized by using a modified solid-state synthesis method. We increased the purity and decreased the synthesis temper-

ature to 200°C by combining mechanical forces with heat to facilitate solid-state diffusion. Details of the synthesis for (18C6@K)$_2$HfBr$_6$ and K$_2$HfBr$_6$ can be found in the supplementary materials.

The crystal structure of (18C6@K)$_2$HfBr$_6$ was determined from single-crystal x-ray diffraction (SCXRD). (18C6@K)$_2$HfBr$_6$ crystallized in the R$\bar{3}$ space group with lattice parameters of a = 14.1332 Å and c = 21.0189 Å (Fig. 1A and table S1). The (18C6@K)$_2$HfBr$_6$ dumbbell structural unit belongs to the S_6 point group, where two K$^+$ cations and the Hf^{4+} cation sit on the S_6 axis. The sixfold symmetry axis of the 18C6 and the S_6 axis of the O$_h$-symmetric [HfBr$_6$]$^{2-}$ octahedron were aligned (Fig. 1B). The K$_2$HfBr$_6$

crystals were face-centered cubic (fcc) (Fig. 1C) (*42*, *43*), in which the [HfBr$_6$]$^{2-}$ ionic octahedra were charge balanced by the surrounding K$^+$ cations (Fig. 1D).

The purity of the (18C6@K)$_2$HfBr$_6$ and K$_2$HfBr$_6$ powders was investigated with powder x-ray diffraction (PXRD) (Fig. 1E). The PXRD pattern of the (18C6@K)$_2$HfBr$_6$ powders matched with the calculated pattern generated from the single-crystal structure with no visible diffraction peaks from impurities. The quality of the PXRD pattern for the K$_2$HfBr$_6$ powders was much lower because of their extreme air sensitivity. The measurement had to be collected in 5 min with an inert atmosphere
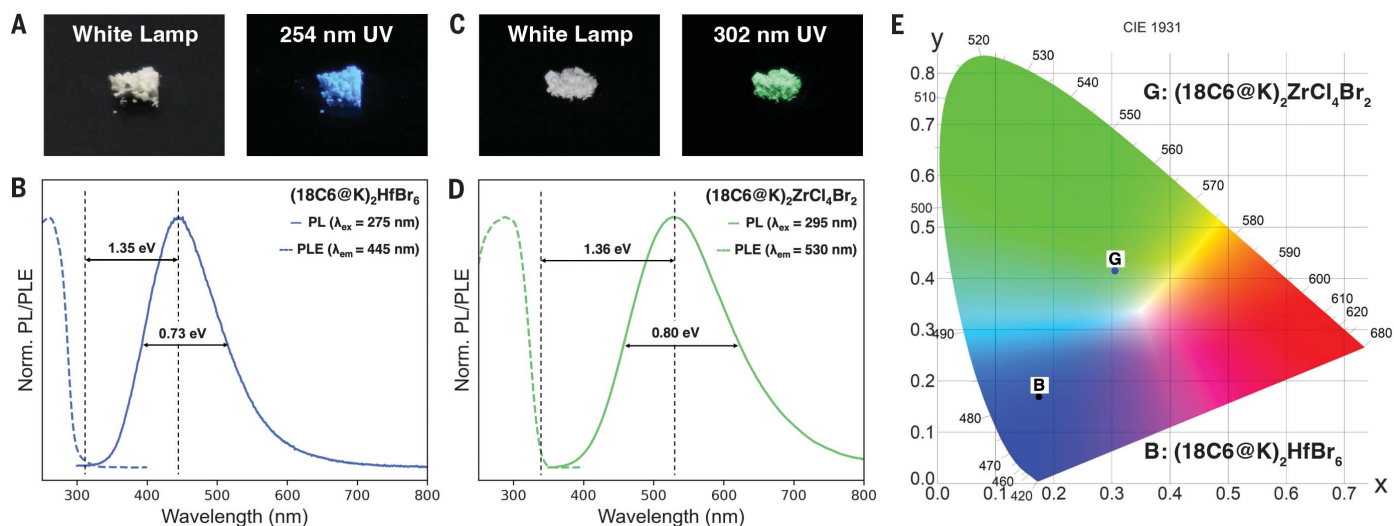
Fig. 2. Blue emission with near-unity PLQY (96.2%) from (18C6@K)$_2$HfBr$_6$ powders and green emission with a PLQY of 82.7% from (18C6@K)$_2$ZrCl$_4$Br$_2$ powders. (**A**) (18C6@K)$_2$HfBr$_6$ powders under white lamp and 254-nm UV excitation. (**B**) PL and PLE spectra of (18C6@K)$_2$HfBr$_6$ powders. (**C**) (18C6@K)$_2$ZrCl$_4$Br$_2$ powders under white lamp and 302-nm UV excitation. (**D**) PL and PLE spectra of (18C6@K)$_2$ZrCl$_4$Br$_2$ powders. (**E**) The CIE 1931 chromaticity diagram for the emission of (18C6@K)$_2$HfBr$_6$ powders and (18C6@K)$_2$ZrCl$_4$Br$_2$ powders. "B" stands for the blue emission of (18C6@K)$_2$HfBr$_6$, and "G" stands for the green emission of (18C6@K)$_2$ZrCl$_4$Br$_2$. The coordinates for the emission colors of (18C6@K)$_2$HfBr$_6$ and (18C6@K)$_2$ZrCl$_4$Br$_2$ were (0.17438, 0.16922) and (0.30597, 0.41533), respectively.

sample holder to prevent the degradation of the powders and measurement of the degradation product. Although the quality of the K$_2$HfBr$_6$ PXRD pattern was not ideal, the most dominant peaks of the fcc K$_2$HfBr$_6$ phase were still identifiable. Moreover, no HfBr$_4$ or KBr diffraction peaks were present (Fig. 1E), which showed that all of the precursor materials transformed into the K$_2$HfBr$_6$ phase. A Raman spectrum of K$_2$HfBr$_6$ further confirmed the presence of the [HfBr$_6$]$^{2-}$ octahedra in the crystal structure (fig. S1).

The crown ether–assisted supramolecular approach was generalized to produce other emissive centers. For example, (18C6@K)$_2$ZrBr$_6$ single crystals and powders were successfully synthesized by the same method, and the same crystal structure as (18C6@K)$_2$HfBr$_6$ was obtained (fig. S2 and table S1). Figure S3 shows that phase-pure (18C6@K)$_2$ZrBr$_6$ powders could be obtained with our established solution-based synthesis. K$_2$ZrBr$_6$ powders were also synthesized with the same solid-state method as K$_2$HfBr$_6$.

The (18C6@K)$_2$HfBr$_6$ and (18C6@K)$_2$ZrBr$_6$ dumbbell building blocks were also the electronic units of the new crystal. To elucidate the effect of 18C6 on the electronic structures of the assembled [HfBr$_6$]$^{2-}$ octahedra, density functional theory (DFT) calculations were performed on (18C6@K)$_2$HfBr$_6$ (Fig. 1F) and K$_2$HfBr$_6$ (Fig. 1G) to determine their electronic band structures and partial electronic density of states (pDOS). The electronic bands of (18C6@K)$_2$HfBr$_6$ were less dispersive compared with K$_2$HfBr$_6$ because the [HfBr$_6$]$^{2-}$ octahedra were more separated in (18C6@K)$_2$HfBr$_6$.

The conduction band (CB) of (18C6@K)$_2$HfBr$_6$ was composed of Hf 5d and Br 4p orbitals, as was the CB of K$_2$HfBr$_6$. However, the valence band (VB) compositions were quite different in these two materials. The VB of K$_2$HfBr$_6$ was mainly composed of the Br 4p orbital, but 18C6 contributed to the VB of (18C6@K)$_2$HfBr$_6$. Thus, the 18C6 molecules were electronically coupled to the [HfBr$_6$]$^{2-}$ octahedra, which indicates that the entire (18C6@K)$_2$HfBr$_6$ dumbbell building block became a new electronic unit. DFT calculations of (18C6@K)$_2$ZrBr$_6$ showed that the contribution from 18C6 to the VB and the band structures were more discrete than those in K$_2$ZrBr$_6$ (fig. S4).

Optical characterization of the blue and green emitters

Compared with K$_2$HfBr$_6$, (18C6@K)$_2$HfBr$_6$ had greatly enhanced emission intensity. Figure 2A shows the extremely bright blue emission of (18C6@K)$_2$HfBr$_6$ powders under 254-nm ultraviolet (UV) excitation. The photoluminescence (PL) spectrum of (18C6@K)$_2$HfBr$_6$ powders was measured at 275-nm excitation (Fig. 2B). The powders had a blue emission centered at 445 nm (2.79 eV), and the full width at half maximum (FWHM) was 0.73 eV. Photoluminescence excitation (PLE) spectra revealed a large Stokes shift (1.35 eV).
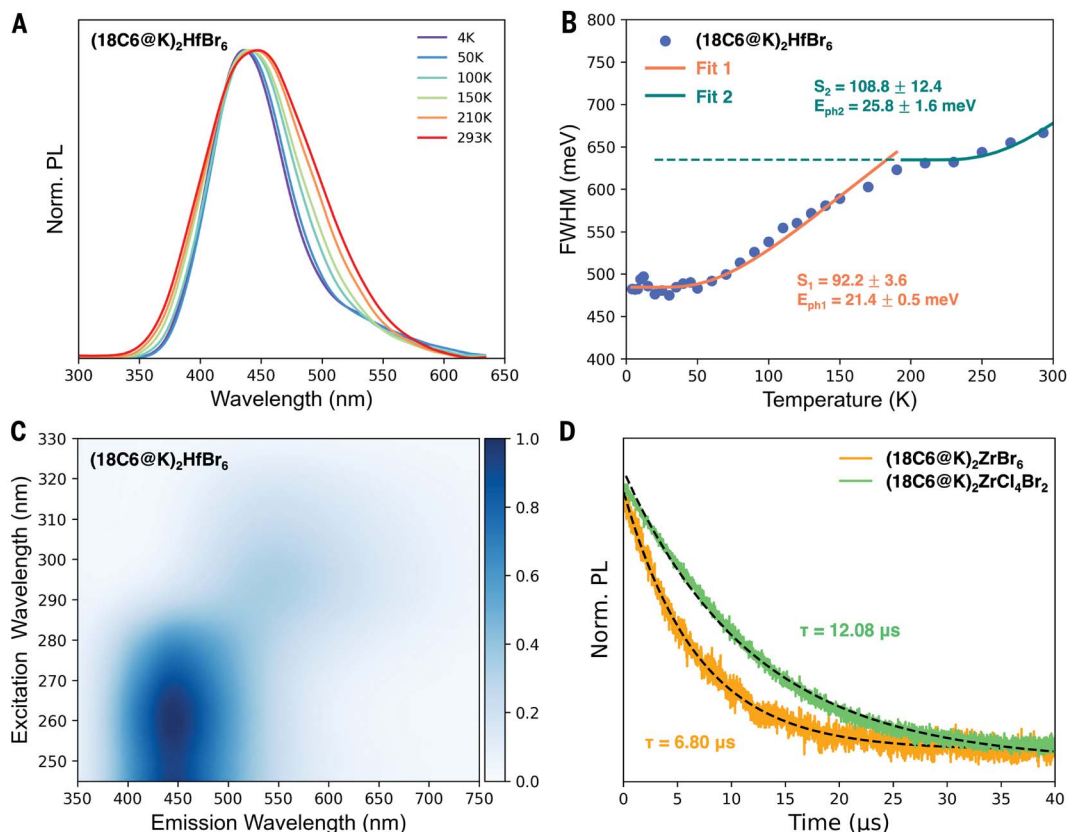
The emission intensity of the (18C6@K)$_2$HfBr$_6$ powders was quantified with PLQY measurement, and a near-unity value of 96.2 ± 1.2% was obtained for the (18C6@K)$_2$HfBr$_6$ powders over six measurements from two batches of samples (fig. S5). The specific value for each measurement is shown in table S2. By contrast, the PLQY of K$_2$HfBr$_6$ powders was 12.8% (fig. S6). K$_2$HfBr$_6$ also had an even larger Stokes shift (1.42 eV) and broader emission, with a peak emission wavelength of 457 nm and a FWHM of 0.90 eV (fig. S7). The color purity of the emission from the [HfBr$_6$]$^{2-}$ octahedra was also enhanced by the supramolecular approach. Figure S8 shows the emission color of (18C6@K)$_2$HfBr$_6$ and K$_2$HfBr$_6$ powders on the CIE 1931 chromaticity diagram. (18C6@K)$_2$HfBr$_6$ had a much purer blue emission color compared with K$_2$HfBr$_6$.

The [ZrBr$_6$]$^{2-}$ units enabled high-PLQY green emissions. Upon 290-nm excitation, (18C6@K)$_2$ZrBr$_6$ had a PL peak at 547 nm, and the FWHM of the PL was 0.69 eV (fig. S9). For the same excitation wavelength, the PL peak of K$_2$ZrBr$_6$ was at 560 nm, and the FWHM of the PL was 0.70 eV (fig. S10). The PLQY of (18C6@K)$_2$ZrBr$_6$ was 49.8% (fig. S11), which was slightly greater than the PLQY of K$_2$ZrBr$_6$ (46.3%) (fig. S12). Although the peak position of the PL spectrum was in the green region, simply analyzing the peak emission wavelength was insufficient given the broadness of the STE-based emission because this crystal actually produced a yellow-green emission color (fig. S13).

Given the great chemical tunability of the dumbbell structural unit, an alloying approach at the halide site was proposed to achieve a purer green emission with near-unity PLQY. For CsPbX$_3$ (where X = Cl$^-$, Br$^-$, or I$^-$) nanocrystals, the emission color can be easily controlled by tuning the halide composition (44); introducing Cl$^-$ in the halide site may generate a shorter wavelength emission color. By carefully tuning the

Fig. 3. Photophysical analysis of (18C6@K)$_2$HfBr$_6$ and (18C6@K)$_2$ZrCl$_4$Br$_2$. (**A**) PL spectra of (18C6@K)$_2$HfBr$_6$ powders at 4, 50, 100, 150, 210, and 293 K. (**B**) FWHM of the PL spectra of (18C6@K)$_2$HfBr$_6$ powders at different temperatures, with the orange and teal solid lines denoting the least-square fit to Eq. 1 at low (4 to 190 K) and high (190 to 293 K) temperature ranges, respectively. (**C**) PLE spectroscopy of (18C6@K)$_2$HfBr$_6$ powders. (**D**) Normalized PL decay curves of (18C6@K)$_2$ZrCl$_4$Br$_2$ and (18C6@K)$_2$ZrBr$_6$ single crystals.

KCl/KBr and ZrCl$_4$/ZrBr$_4$ precursor ratio in the synthesis, the Cl$^-$/Br$^-$ ratio in the obtained (18C6@K)$_2$ZrX$_6$ dumbbell structural unit can be precisely controlled. As expected, a larger Cl$^-$/Br$^-$ ratio created a more blue-shifted PL (figs. S14 and S15). For example, (18C6@K)$_2$ZrCl$_3$Br$_3$ and (18C6@K)$_2$ZrCl$_4$Br$_2$ had green emission with PL peaks at 534 and 530 nm, respectively. Increasing the Cl$^-$ content to a composition of (18C6@K)$_2$ZrCl$_{4.5}$Br$_{1.5}$ changed the PL color to a cyan (bluish green) color. The established halide site alloying approach not only generated a purer green emission color but also boosted the PLQY of the emission to near-unity. For the Cl$^-$/Br$^-$ ratio from 1:1 to 2:1 to 3:1, the PLQYs were 69.1, 82.7, and 87.0%, respectively (figs. S16 and S17).

Because the 2:1 Cl$^-$/Br$^-$ ratio composition had both pure-green emission color and high PLQY, we selected (18C6@K)$_2$ZrCl$_4$Br$_2$ for detailed studies of green emission. (18C6@K)$_2$ZrCl$_4$Br$_2$ single crystals were synthesized by controlling the Cl$^-$/Br$^-$ precursor ratio to be 2:1. The formula of (18C6@K)$_2$ZrCl$_4$Br$_2$ was determined by SCXRD (Cl$^-$:Br$^-$ = 4.3:1.7) (fig. S18 and table S3) and energy-dispersive x-ray spectroscopy (EDX) elemental mapping (Cl$^-$:Br$^-$ = 4.1:1.9) (fig. S19). The Cl and Br atoms were perfectly miscible in the crystal structure. PXRD of the (18C6@K)$_2$ZrCl$_4$Br$_2$ powders (fig. S20) also indicated that this composition was a phase-pure

system. The (101) and (110) diffraction peaks of (18C6@K)$_2$ZrCl$_4$Br$_2$ were slightly shifted to larger 2θ values compared with the corresponding PXRD peaks of (18C6@K)$_2$ZrBr$_6$, which suggests smaller lattice constants (fig. S21).

Figure 2C shows the bright green emission of (18C6@K)$_2$ZrCl$_4$Br$_2$ powders under 302-nm UV lamp excitation. The PL spectrum of (18C6@K)$_2$ZrCl$_4$Br$_2$ powders was measured at 295-nm excitation (Fig. 2D). The green emission had a similar Stokes shift (1.36 eV versus 1.35 eV) and FWHM (0.80 eV versus 0.73 eV) compared to the blue emission of the (18C6@K)$_2$HfBr$_6$ powders, which suggests similar emission properties of the Hf and Zr metal centers in the supramolecular assembly materials system. The PLQY of the emission from (18C6@K)$_2$ZrCl$_4$Br$_2$ powders was 82.7 ± 0.9%, which was determined through the measurement of four samples from two batches (table S4). Therefore, we achieved highly emissive powders with blue and green emission colors based on the supramolecular assembly approach. The blue and green colors of the emissions from (18C6@K)$_2$HfBr$_6$ and (18C6@K)$_2$ZrCl$_4$Br$_2$, respectively, are summarized in the CIE 1931 diagram (Fig. 2E).

Next, we conducted a comprehensive photophysics analysis to confirm and gain deeper insights into the STE emission mechanism that underlies these blue and green emissions. The distinctive features of STE emissions, in-

cluding their large Stokes shift and broadband nature, are primarily attributed to the electron-phonon coupling effect. To unravel the STE emission mechanism, we performed low-temperature PL measurements to examine the electron-phonon coupling in (18C6@K)$_2$HfBr$_6$. With increasing temperatures, the PL peak gradually broadened, and the peak was slightly red-shifted, indicating greater phonon participation at higher temperatures (Fig. 3A). A small shoulder peak at ~550 nm was present that was especially distinct at lower temperatures, which we attribute to the Zr impurity in the HfBr$_4$ precursor (35). Inductively coupled atomic emission spectroscopy revealed an ~0.5 atomic % (at %) ZrBr$_4$ impurity in the as-obtained HfBr$_4$ precursor, and that there was an ~0.6 at % Zr^{4+} impurity in the synthesized (18C6@K)$_2$HfBr$_6$ single crystals (table S5).

To deconvolve the emission from (18C6@K)$_2$ZrBr$_6$ impurities, a two-peak Gaussian fitting was applied to the PL spectrum at each temperature. Figure S22 shows an example at 4 K. The FWHMs of the (18C6@K)$_2$HfBr$_6$ peaks were obtained from the Gaussian fittings and are summarized in table S6. The temperature dependence of the FWHM of the emission peak was modeled using the theory of Toyozawa (45), which applies a configuration coordinate model to explain the broadening of the emission originating from electron-phonon

coupling. The FWHM depends on the Boltzmann constant k_B, the effective phonon energy E_{ph}, the temperature T, and the Huang-Rhys electron-phonon coupling parameter S (46)

$$\text{FWHM} = 2.36\sqrt{S}E_{ph}\sqrt{\coth\frac{E_{ph}}{2k_BT}} \quad (1)$$

The relation between FWHM and temperature is shown in Fig. 3B. Analyzing the data according to Eq. 1 yielded a coupling factor $S_1 = 92.2 \pm 3.6$ and an effective phonon energy $E_{ph1} = 21.4 \pm 0.5$ meV. This phonon mode corresponded to the asymmetric stretching mode (E_g) of the $[HfBr_6]^{2-}$ octahedra, which was observed at 20.4 meV (164.5 cm^{-1}) in the Raman spectrum (fig. S23). However, this pho-

non mode was only responsible for STE formation up to 190 K. For temperatures >190 K, a higher energy phonon mode dominated STE formation.

Shifting the zero temperature of Eq. 1 by 190 K, a second fit could be obtained with a coupling factor $S_2 = 108.8 \pm 12.4$ and an effective phonon energy $E_{ph2} = 25.8 \pm 1.6$ meV. This phonon mode corresponded to the sym-

Fig. 4. Solution processability and display application of highly emissive blue and green semiconductor inks. (**A**) Schematic illustrating the thin-film fabrication method and the display application. The inks were formed by mixing (18C6@K)$_2$HfBr$_6$ or (18C6@K)$_2$ZrCl$_4$Br$_2$ powders and PS in DCM. Thin films were obtained by drop casting, and they demonstrated programmable display capability. DMD, digital micromirror device. (**B**) (18C6@K)$_2$HfBr$_6$/PS-DCM ink under white light and 254-nm UV lamp excitation. (**C**) (18C6@K)$_2$ZrCl$_4$Br$_2$/PS-DCM ink under white light and 302-nm lamp excitation. (**D**) (18C6@K)$_2$HfBr$_6$/PS composite thin film under white light and 254-nm UV excitation. (**E**) (18C6@K)$_2$ZrCl$_4$Br$_2$/PS composite thin film under white light and 302-nm UV excitation. The scale bars for (B) to (E) are 1 cm. The PLQYs of all samples are shown in the photos. (**F**) Image of the "Cal" logo blue emission on the (18C6@K)$_2$HfBr$_6$/PS composite thin film. (**G**) Snapshots of a video showing the alphabet, A to Z, with 0.1 s per letter on the (18C6@K)$_2$HfBr$_6$/PS composite thin film. The scale bars for (F) and (G) are 3 mm and 4 mm, respectively.

metric stretching mode (A_{1g}) of the $[HfBr_6]^{2-}$ octahedra at 25.1 meV (202.5 cm^{-1}). The large Huang-Rhys factor S in both scenarios indicated a very strong electron-phonon coupling in this material. For example, S for CsPbX$_3$ (where X = Br$^-$ or I$^-$) is <1 (47), and the S for double perovskite Cs$_2$AgBiBr$_6$ is only ~12 (48). STE behavior is closely related to the octahedra packing dimensionality. Through our supramolecular approach, the $[HfBr_6]^{2-}$ octahedra were more isolated by the bulky $(18C6@K)^+$ complexes, which led to stronger self-trapping with larger S values.

Excitation wavelength–dependent PL mapping of (18C6@K)$_2$HfBr$_6$ (Fig. 3C) showed that for excitation wavelengths <285 nm, a broad PL peak at 445 nm emerged. The PL peak position and shape were independent of the excitation wavelength <285 nm. Thus, for above-bandgap excitation, the emission originated from the relaxation of the same excited state. However, for excitation wavelengths >285 nm, a much weaker PL peak at ~550 nm replaced the previous PL peak that arose from the ~0.6 at % (18C6@K)$_2$ZrBr$_6$ impurity, and 2D PLE mapping of (18C6@K)$_2$ZrBr$_6$ showed a single PL peak at ~550 nm from 245-nm to 330-nm excitation (fig. S24).

Time-resolved PL (TRPL) studies on the supramolecular assembled single crystals revealed that the PL decay of the (18C6@K)$_2$ZrBr$_6$ could be mostly described by a monoexponential decay profile on the microsecond timescale, with a PL lifetime of 6.80 μs (Fig. 3D and table S7). By contrast, Cs$_2$ZrBr$_6$ bulk crystal featured a triple-exponential PL decay, yielding decay time constants of 40 ns (8.9%), 0.99 μs (24%), and 4.6 μs (68%) (35). Additionally, Cs$_2$ZrBr$_6$ nano-crystals showed a double-exponential PL decay with time constants at 0.78 and 4.5 μs (49). The PLQY was related to both the radiative and nonradiative decay rates [PLQY = $k_{rad}/(k_{rad} + k_{nonrad})$], so a more sluggish radiative decay did not necessarily correlate to a lower PLQY. Notably, the PLQY of (18C6@K)$_2$ZrBr$_6$ powders (49.8%) was greater than that of K$_2$ZrBr$_6$ powders (46.3%, from our measurement) and Cs$_2$ZrBr$_6$ nanocrystals [~44%, from (49)]. This observation suggested that the nonradiative decay rate of the supramolecular sample was slower than that of the vacancy-ordered double perovskite phases and may indicate a lower defect density in our assembled crystals. The PL decay of the (18C6@K)$_2$ZrCl$_4$Br$_2$ single crystal could also be fit with a single exponential function with an even longer PL lifetime (12.08 μs) (Fig. 3D and table S8). Cs$_2$ZrCl$_6$ had a slightly longer PL lifetime (7.5 μs) compared with that of Cs$_2$ZrBr$_6$ (50). This result suggested that the supramolecular material system had a longer PL lifetime and slower nonradiative decay rate.

We also evaluated the photostability of these highly emissive blue and green emitters. Notably, previous research in the organic light-

emitting diode (OLED) community has used a xenon lamp to simulate solar irradiation, dissolving Ir complexes in deuterated toluene for reference measurements of green and blue emission (51, 52). To ensure a fair comparison, we applied identical irradiation energy density (62 mW/cm^2) and temperature (35°C), and deuterated toluene was used to disperse the (18C6@K)$_2$HfBr$_6$ and (18C6@K)$_2$ZrCl$_4$Br$_2$ powders. Figure S25 shows the PL intensity decay of the (18C6@K)$_2$HfBr$_6$ and (18C6@K)$_2$ZrCl$_4$Br$_2$ samples under continuous irradiation. Both decay trends could be accurately described by the integrated rate law for the first-order reaction [ln(I_t/I_0) = $-kt$]. The rate constants of photodegradation were estimated to be 5.1 × 10^{-3} h^{-1} and 3.0 × 10^{-3} h^{-1} for (18C6@K)$_2$HfBr$_6$ and (18C6@K)$_2$ZrCl$_4$Br$_2$, respectively. Notably, even under stringent irradiation conditions, the PL intensities of (18C6@K)$_2$HfBr$_6$ and (18C6@K)$_2$ZrCl$_4$Br$_2$ decreased to 80% after 43 and 73 hours, respectively. These findings underscore the superior photostability of the supramolecular assembled samples compared with most Ir complexes, rivaling the best-reported green-emitting fac-[Ir(ppy)$_3$] reference (k = 2.6 × 10^{-3} h^{-1}) (51, 52). Previous studies on the photodegradation of the Ir complexes, such as Ir(ppy)$_3$ and Ir(piq)$_3$, have identified singlet oxygen attack and interaction of the excited-state molecule with its local environment as primary degradation pathways (53).

Blue-green dual-color display and 3D printing

The high PLQY of the blue and green emission colors in the powders were preserved in thin films, which would enable various optoelectronic device applications (54–56). Because the powders were stable in nonpolar organic solvents, they could be evenly dispersed into solution to form inks. We used DCM because its low boiling point (39.6°C) leads to high volatility for drying films, and we added PS to create inks suitable for drop casting or spin coating by increasing the viscosity (Fig. 4A) (57, 58). The image of (18C6@K)$_2$HfBr$_6$/PS ink under a white lamp (Fig. 4B) shows that a uniform white suspension was achieved that exhibited a bright blue emission under 254-nm excitation. The emission was solely from the (18C6@K)$_2$HfBr$_6$ powders in the ink because the shape of the PL spectrum was the same as the PL shape of the powders (fig. S26). The solution PLQY was 90.8% (Fig. 4B and fig. S27), which was only 5.5% less than the powder PLQY. This reduction was expected because DCM and PS do not absorb strongly in the blue color wavelength region (fig. S28), and the suspended powders in the ink could cause losses through scattering. The (18C6@K)$_2$ZrCl$_4$Br$_2$/PS ink also preserved the green emission of the (18C6@K)$_2$ZrCl$_4$Br$_2$ powders with a solution PLQY of 75.0% (Fig. 4C and fig. S29).

The inks could be drop casted under ambient conditions, and, after rapid solvent evaporation, a uniform thin film forms (Fig. 4, A, D, and E). PXRD patterns of the (18C6@K)$_2$HfBr$_6$/PS composite (fig. S30) and the (18C6@K)$_2$ZrCl$_4$Br$_2$/PS composite (fig. S31) showed that the structural integrity of the powders was preserved in the PS matrix. Scanning electron microscopy (SEM) imaging of the (18C6@K)$_2$HfBr$_6$ powders and the (18C6@K)$_2$HfBr$_6$/PS composite thin-film surface (fig. S32) indicated that the submicrometer-sized powders were uniformly dispersed. Cross-sectional SEM imaging of the thin film (fig. S33) proved the presence and uniformity of the powders across the thin film. Under UV irradiation, (18C6@K)$_2$HfBr$_6$/PS and (18C6@K)$_2$ZrCl$_4$Br$_2$/PS composite thin films showed bright blue and green emissions, respectively (Fig. 4, D and E). The shapes of the PL spectra of the thin films were the same as those for the powders (figs. S25 and S34), and the PLQYs were 80.3% (fig. S35) and 69.0% (fig. S36) for blue- and green-emitting composites, respectively.

The stability of the air-sensitive Hf and Zr octahedral clusters was further enhanced in the PS polymer composite. Both Cs$_2$HfBr$_6$ and Cs$_2$ZrBr$_6$ double-perovskite structures are predicted to be thermodynamically unstable in the presence of water and oxygen (37), and we found that K$_2$HfBr$_6$ and K$_2$ZrBr$_6$ powders turn from a white to a brownish color after a few minutes of air exposure and became nonemissive. By contrast, the (18C6@K)$_2$HfBr$_6$/PS and (18C6@K)$_2$ZrCl$_4$Br$_2$/PS composites maintained their blue and green emission colors, respectively, after 1 month of storage in the air (fig. S37). The air-stable PS polymers along with the hydrophobic crown ethers could greatly protect the air-sensitive Hf and Zr metal emission centers.

We explored display applications of the powder-PS composite thin films. A digital mirror device with a pixel resolution of 2560 by 1440 sequentially patterned 250-nm UV light through projection optics onto the (18C6@K)$_2$HfBr$_6$/PS composite thin film with a spot size of 6.9 by 3.9 mm at a frame rate of 60 Hz (schematic of the process is illustrated in Fig. 4A). An emissive blue "Cal" logo was illuminated on the thin film with dimensions 3.8 mm in height and 4.7 mm in width (Fig. 4F). The logo exhibited high luminosity characterized by sharply defined edges. To further demonstrate dynamically changing display luminescence, we illuminated the alphabet sequence (from A to Z) onto the thin film with a fast flipping rate (0.1 s per letter). A video of 2.6 s was recorded (movie S1). Although the duration of each letter was very short, the blue emission with the shape of the letters was sharp and bright, as illustrated in the snapshot photos (Fig. 4G). The size of the letters was only 3.1 mm in width and 3.9 mm in length, but every feature of the letters was clearly visible with similar emission intensity
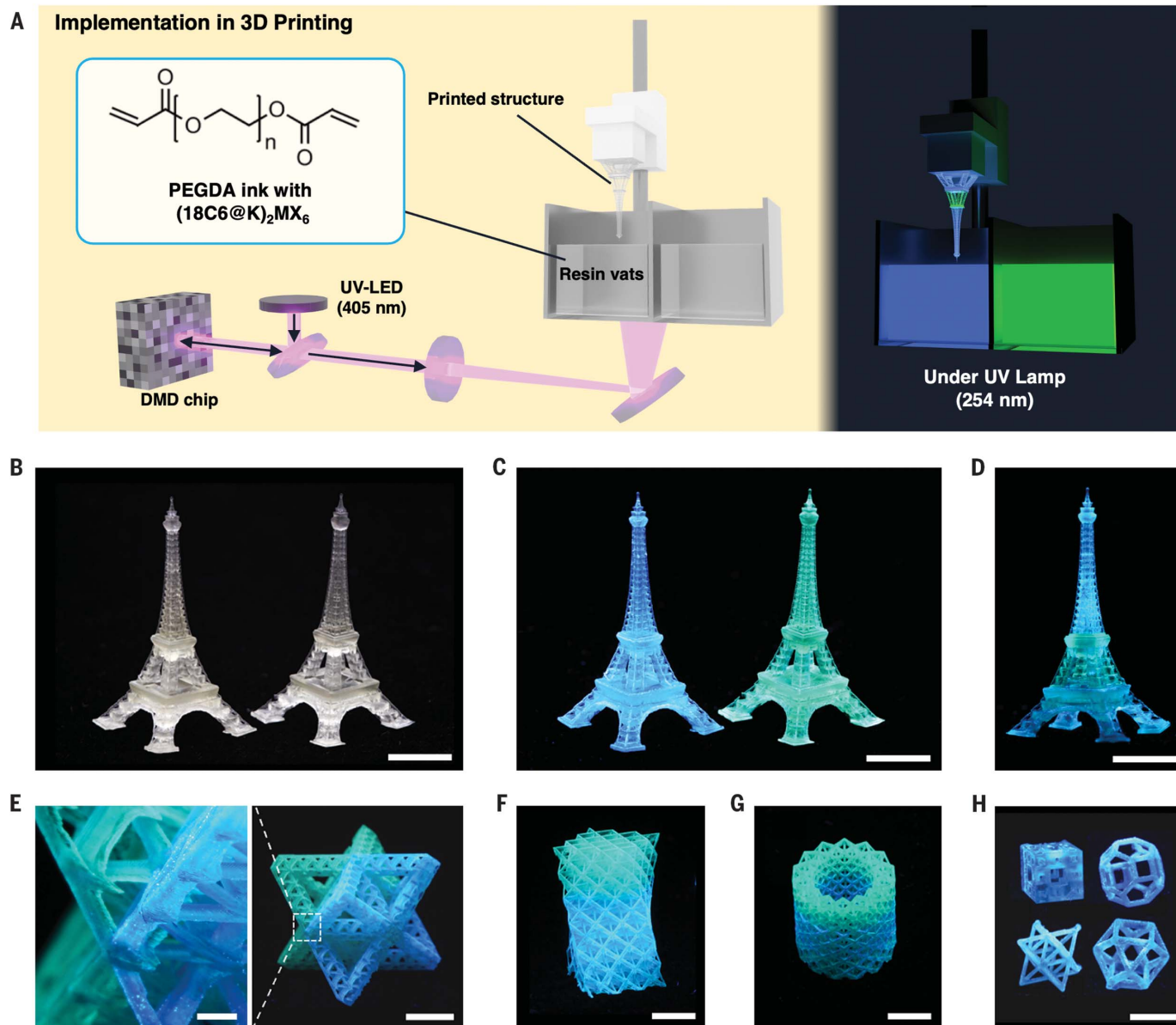
Fig. 5. Implementation of the blue-green dual-color 3D printing. (**A**) Schematic illustrating the multimaterial 3D printing process. (**B** and **C**) Two 3D-printed light-emitting Eiffel Towers under white light (B) and 254-nm UV (C) excitation. (**D**) A dual-color–emitting Eiffel Tower under 254-nm UV excitation. (**E** to **H**) Conformal and twisted octet trusses with varying hierarchical structures and geometric shapes, including cuboctahedron, tetrakaidecahedron, and Menger sponge structures, with the blue and green emitters or their combinations, respectively. These printed architectures were photoexcited at 254 nm. The scale bars for (B) to (G) are 5 mm. The scale bar for the zoom-in image of (E) is 0.6 mm. The scale bar for (H) is 4 mm.

owing to the high uniformity of the thin film. Furthermore, the response time of the display should be fast because the PL decay rate of the $(18C6@K)_2HfBr_6$ powders was ~3 orders of magnitude faster than the frame rate of the digital mirror device. The letters switch extremely fast, with no blurring, ghosting, or trailing effects.

These emissive powders could also be processed with high-resolution 3D printing technologies after blending them uniformly into a monomer resin. Conventional resins for 3D printing typically use dyes as the photoabsorber to control the depth of UV penetration

and, consequently, the printing resolution. However, dyes absorb light and color the final printed parts. To avoid interference with our blue and green emitters, we developed a photoabsorber-free resin mainly composed of photomonomer poly(ethylene glycol) diacrylate (PEGDA) but with a high content of photoinhibitor to control the printing resolution. The polymerized PEGDA resin exhibited minimal absorption within the visible spectrum, featuring a modest absorption peak from 355 to 425 nm (fig. S38A). Also, under 250-nm UV excitation, the resin exhibited substantially low emission intensity (fig. S38B). Hence, the emission colors

in the blue and green range of our emitters remained largely unaffected.

Upon stirring and sonication, the powders were uniformly dispersed into the PEGDA resin. We exploited a multimaterial digital light-printing method (*59*, *60*) to achieve a 3D assembly of the blue and green emitters into complex macro- and microarchitectures. Under 405-nm structured UV light illumination, the resin rapidly converted into solid 3D structures (Fig. 5A). The PL spectra from the $(18C6@K)_2HfBr_6/PEGDA$ and the $(18C6@K)_2ZrCl_4Br_2/PEGDA$ composites were similar to those of the powders (fig. S38, C and D; fig. S39; and fig. S40). The printed

architectural models of the Eiffel Tower (Fig. 5B), after excitation at 254 nm, showed their respective blue and green colors (Fig. 5C). The dimensions of the two Eiffel Towers were within a few centimeters, with high-resolution spatial features (Fig. 5B). The submicrometer scale of these powders and a printing layer thickness of 40 µm enabled even distribution throughout each layer and ensured a homogeneous emission color profile across the entire architectural construct.

A single 3D-printed structure could also manifest emissions in both blue and green by alternative resins during the printing procedure. An Eiffel Tower design characterized by blue emissions at its upper and lower segments with green emissions in its central region is shown in Fig. 5D, and a second-order hierarchical lattice structure (octet truss) was realized with one half radiating in blue and the other in green (Fig. 5E). Notably, a close-up view of the boundary between these blue- and green-emitting regions within the octet truss structure revealed the high precision in color transition without any color crossover on either side. Twisted (Fig. 5F and fig. S41) and conformal (Fig. 5G and fig. S42) octet truss architectures with dual emissions were also achieved with bright emissions and high structural accuracy.

Other complex topologies, such as cuboctahedron, tetrakaidecahedron, octet truss, and Menger sponge with the blue emitter embedded (Fig. 5H and figs. S43 and S44), were also obtained to exhibit the variety of structures that could be printed with the light-emitting ink. These demonstrations served as a proof of concept for integrating emissive ionic powders with 3D printing technology. The potential applications of 3D-printed light-emitting structures are extensive and constantly evolving, ranging from intricate interior ambient-lighting solutions to seamless integration into wearable devices.

Discussion

We have demonstrated a supramolecular assembly strategy for achieving halide perovskite blue and green emitters with ultrahigh PLQYs. Specifically, $(18C6@K)_2HfBr_6$ warranted a blue emission with a near-unity (96.2%) PLQY, and $(18C6@K)_2ZrCl_4Br_2$ showed a green emission with a PLQY of 82.7%. The emission of the supramolecular assembled samples originated from the STE emission, with strong electron-phonon coupling and microsecond PL lifetimes. The supramolecular approach is very promising for solution processability. The $(18C6@K)_2HfBr_6$/PS-DCM ink maintained a high PLQY of >90%. Uniform thin films were fabricated from this ink through a drop-casting technique. The $(18C6@K)_2HfBr_6$/PS composite had blue emission with a PLQY of >80%, making it favorable for patterning, display,

and printing applications. The powders with blue and green emissions were also highly compatible with the 3D printing technology. The supramolecular assembly approach for halide perovskite building block catalyzes further investigation into the synthesis and characterization of supramolecular assembled functional materials, laying the foundation for substantial progress in the field.

REFERENCES AND NOTES

1. M. A. Reshchikov et al., J. Appl. Phys. **111**, 073106 (2012).
2. M. A. Reshchikov, R. Y. Korotkov, Phys. Rev. B **64**, 115205 (2001).
3. A. K. Viswanath, J. I. Lee, D. Kim, C. R. Lee, J. Y. Leem, Phys. Rev. B **58**, 16333–16339 (1998).
4. W. Shan et al., Phys. Rev. B **54**, 16369–16372 (1996).
5. C. Hauswald et al., Phys. Rev. B **90**, 165304 (2014).
6. M. Shibata, T. Furuya, H. Sakaguchi, S. Kuma, J. Cryst. Growth **196**, 47–52 (1999).
7. W.-J. Yin, T. Shi, Y. Yan, Appl. Phys. Lett. **104**, 063903 (2014).
8. R. J. Sutton et al., Adv. Energy Mater. **6**, 1502458 (2016).
9. M. R. Filip, G. E. Eperon, H. J. Snaith, F. Giustino, Nat. Commun. **5**, 5757 (2014).
10. L. Protesescu et al., Nano Lett. **15**, 3692–3696 (2015).
11. J. Kang, L.-W. Wang, J. Phys. Chem. Lett. **8**, 489–493 (2017).
12. K. X. Steirer et al., ACS Energy Lett. **1**, 360–366 (2016).
13. F. Deschler et al., J. Phys. Chem. Lett. **5**, 1421–1426 (2014).
14. F. Di Stasio, S. Christodoulou, N. Huo, G. Konstantatos, Chem. Mater. **29**, 7663–7667 (2017).
15. J. Li, L. Gan, Z. Fang, H. He, Z. Ye, J. Phys. Chem. Lett. **8**, 6002–6008 (2017).
16. S. Wang, C. Bi, J. Yuan, L. Zhang, J. Tian, ACS Energy Lett. **3**, 245–251 (2018).
17. X. Gong et al., Nat. Mater. **17**, 550–556 (2018).
18. H. Luo, Y. Huang, H. Liu, B. Zhang, J. Song, Chem. Eng. J. **430**, 132790 (2022).
19. M. C. Folgueras et al., Nano Lett. **21**, 8856–8862 (2021).
20. J. Jin et al., Nano Lett. **21**, 5415–5421 (2021).
21. M. Gao et al., Matter **4**, 3874–3896 (2021).
22. J. S. Manser, M. I. Saidaminov, J. A. Christians, O. M. Bakr, P. V. Kamat, Acc. Chem. Res. **49**, 330–338 (2016).
23. M. C. Folgueras et al., J. Phys. Chem. C **125**, 25126–25139 (2021).
24. D. Ju et al., ACS Energy Lett. **4**, 228–234 (2019).
25. A. D. Nicholas, B. W. Walusiak, L. C. Garman, M. N. Huda, C. L. Cahill, J. Mater. Chem. C **9**, 3271–3286 (2021).
26. J. Zhou et al., Adv. Opt. Mater. **7**, 1900139 (2019).
27. Z. Tan et al., Adv. Mater. **32**, 2002443 (2020).
28. H. Yin et al., Angew. Chem. Int. Ed. **60**, 22693–22699 (2021).
29. I. N. Douglas, J. V. Nicholas, B. G. Wybourne, J. Chem. Phys. **48**, 1415–1416 (1968).
30. C. Li et al., Acta Cryst. **B64**, 702–707 (2008).
31. Q. He et al., ACS Mater. Lett. **2**, 633–638 (2020).
32. C. Zhou et al., Chem. Sci. **9**, 586–593 (2017).
33. M. Li, Z. Xia, Chem. Soc. Rev. **50**, 2626–2662 (2021).
34. J. A. Steele et al., ACS Nano **12**, 8081–8090 (2018).
35. K. Saeki et al., Jpn. J. Appl. Phys. **57**, 030310 (2018).
36. A. Abfalterer et al., ACS Mater. Lett. **2**, 1644–1652 (2020).
37. C. Kaewmeechai, Y. Laosiritaworn, A. P. Jaroenjittichai, Results Phys. **30**, 104875 (2021).
38. W. Thomas, H. Elias, J. Inorg. Nucl. Chem. **38**, 2227–2229 (1976).
39. E. V. van Loef, G. Ciampi, U. Shirwadkar, L. Soundara Pandian, K. S. Shah, J. Cryst. Growth **532**, 125438 (2020).
40. S. Kodama et al., Opt. Mater. **106**, 109942 (2020).
41. C. Zhu et al., J. Am. Chem. Soc. **144**, 12450–12458 (2022).
42. J. E. Saal, S. Kirklin, M. Aykol, B. Meredig, C. Wolverton, J. Miner. Met. Mater. Soc. **65**, 1501–1509 (2013).
43. S. Kirklin et al., NPJ Comput. Mater. **1**, 15010 (2015).
44. Q. A. Akkerman et al., J. Am. Chem. Soc. **137**, 10276–10281 (2015).
45. Y. Toyozawa, Prog. Theor. Phys. **27**, 89–104 (1962).
46. W. Stadler et al., Phys. Rev. B **51**, 10619–10630 (1995).
47. Y. Song et al., Mater. Res. Express **6**, 115064 (2019).
48. S. J. Zelewski et al., J. Mater. Chem. C **7**, 8350–8356 (2019).
49. V. Vaněček et al., J. Cryst. Growth **573**, 126307 (2021).
50. K. Saeki, Y. Fujimoto, M. Koshimizu, T. Yanagida, K. Asai, Appl. Phys. Express **9**, 042602 (2016).
51. H.-H. Kuo et al., Adv. Sci. **5**, 1800846 (2018).
52. H.-H. Kuo et al., J. Mater. Chem. C **6**, 10486–10496 (2018).
53. S. Schmidbauer, A. Hohenleutner, B. König, Beilstein J. Org. Chem. **9**, 2088–2096 (2013).
54. W. Hui et al., Science **371**, 1359–1364 (2021).
55. F. Mathies et al., J. Mater. Chem. A **4**, 19207–19213 (2016).
56. S. X. Li et al., ACS Appl. Mater. Interfaces **13**, 31919–31927 (2021).
57. M. Kaseem, K. Hamad, Y. G. Ko, Eur. Polym. J. **79**, 36–62 (2016).
58. Y. Tu et al., J. Mater. Chem. **20**, 1594–1599 (2010).
59. H. Cui et al., Science **376**, 1287–1293 (2022).
60. R. Hensleigh et al., Nat. Electron. **3**, 216–224 (2020).